24 SI Materials & Methods

25 Animals

26 All mice tested were obtained by internal colonies from the European Molecular biology

27 laboratory. Mice were maintained in temperature and humidity-controlled condition with

28 food and water provided *ad libitum* and on 12-h light-dark cycle (light on at 7:00). *C57BL/6J*

29 mice were obtained from local EMBL Rome colonies. The following transgenic mice lines

30 were used: *Thy1*::EGFP-M (1) (Jackson Laboratory stock 007788) and *Rosa26-CAG::loxP-*

31 *STOP-loxP-tdTomatoWPRE (2)* (Jackson Laboratory stock 007905), CD11b-deficient mice

32 (3) (*C3r* or *Itgam*) (Jackson Laboratory stock 003991), *Emx1::Cre (4)*. Thy1::EGFP animals

33 were bred with *C3r* mice to generate double transgenic mice. Animals homozygous for

34 *Thy1::*EGFP and heterozygous for *C3r* were bred to get animals of the desired genotype.

35 Heterozygote *C3r* animals were bred to obtain WT controls and KO animals. For all the

36 experiments littermate WT and KO were used wherever possible. Both males and females

37 were used indiscriminately. All experiments were performed in accordance 91 with EU

38 Directive 2010/63/EU and under approval of the EMBL Animal Use Committee 392 and

39 Italian Ministry of Health License 541/2015-PR to C.G. The fMRI experiments were

40 conducted in accordance with EU 86/609/EEC, DL 116, January 1992 and the Guide for the

41 Care and use of Laboratory Animals of the National Institutes of Health. All surgical

42 procedures were performed under anesthesia.

43 In vivo PSVue labelling

44 The activated PSVue 550 was prepared according to manufacturer's instructions (Molecular

45 Targeting Technologies) using Zinc Nitrate and diluted to 1mM using sterile water. For *in*

46 *vivo* labelling of apoptotic cells, postnatal day 4 pups were anesthetized by placing on

47 crushed ice for 2-3 mins. Animals were then placed on a custom stage and the head was

48 illuminated with a fibre optic light source. 1µl of activated PSVue was injected into the

49 lateral ventricles (2/5th of the distance from the lambda to eye) using a 32G Hamilton syringe

50 and the syringe was left in place 20-30 secs after injection. The pups were placed under a

51 warm lamp and returned to the dam after recovery. 24 hours after injection the pups were

52 perfused intracardially with PBS and 4% PFA in the Phosphate buffer. The brains were post-

53 fixed in 4% PFA overnight and transferred to 30% Sucrose for cryoprotection

54   *Immunostaining*

55   For immunostaining of cryostat sections (40µm or 30; Leica Microsystems) were incubated

56   with blocking buffer (1x PBS + 2% BSA + 0.3% Triton X-100) for 2 hours followed by

57   overnight incubation at 4°C with primary antibodies diluted in blocking buffer. The following

58   antibodies were used: Goat anti-Iba1, Wako 011-27991, 1:250, Rabbit anti-activated caspase-

59   3, Cell Signaling Technologies, 1:500, Rabbit anti-Iba1, Wako 019-19741, 1:500, Mouse

60   anti-NeuN, Millipore MAB377, 1:200. For spine density analysis, Thy1::EGFP labeled

61   Vibratome sections (50µm; Leica Microsystems) were blocked and then incubated overnight

62   at 4°C with primary antibody (Chicken anti-GFP, Aves Lab 1:500) diluted in blocking buffer.

63   Following incubation with primary antibody the tissues were washed in PBS, blocked and

64   incubated with fluorophore conjugated secondary antibodies (Life Technologies) for 2 hours

65   at room temperature. The tissues were mounted with MOWIOL or Prolong (Life

66   Technologies).

67   *Electron microscopy and quantification of optic nerve*

68   Mice at postnatal day six, from five different litters, were deeply anesthetized with Avertin

69   (400 mg/kg, i.p.; Sigma-Aldrich) and slowly (less than 1ml/min) perfused transcardially with

70   1x PBS and then 4% paraformaldehyde plus 2.5% Glutaraldehyde in 0.1 M phosphate buffer

71   (PB), pH 7.4. Eyes were promptly extracted and the part of optic nerves attached (preceding

72   the optic chiasm) dissected and placed in post-fixation buffer overnight (4%

73   paraformaldehyde plus 2.5% Glutaraldehyde in 0.1 M phosphate buffer, pH 7.4). Any nerves

74   that showed signs of damage were discarded. Samples were then shipped to Electron

75   Microscopy Core facility site in EMBL-Heidelberg, for imaging, in 0.1M PB solution

76   containing 0.5x fixative and with no air to avoid oxidation. Samples were then prepared for

77   imaging: with 1% OsO4/1.5% Potassium Ferrocyanide for 1h on ice, then with 1% OsO4 in

78   Sodium Cacodylate buffer 0.1M pH 7.4 on ice followed by 10x rinse in water and then

79   stained in with 1% aqueous solution of Uranyl Acetate overnight at 4°C. Samples were then

80   dehydrated with increasing concentration of Ethanol and after 100% Ethanol they were

81   infiltrated in 3:1, 1:1 and 3:1 acetone:resin for 2h each step, and left in 100% resin overnight

82   rotating. Samples were embedded into molds the next morning. Durcupan embedding was

83   carried out in a flat orientation within a sandwich of ACLAR® 33C Films (Electron

84   Microscopy Science) for 72h at 60°C. The samples were then cut and remounted on EPON

85   blocks for sectioning.

Sections 90 nm thick were collected in the middle region of the optic nerve extracted (by avoiding the damaged extremities) and post-stained for 3 min with lead citrate. Images were acquired on a JEOL JEM-2100 Plus electron microscope at 120 kV with the SHOTMEISTER (JEOL software) and then collected and shared with LLP Viewer software. Montages were taken at 1200x and 5000x magnification.

The regions of interest selected along the vertical midline, over the longer axes of optic nerves, were exported in Fiji with a fixed width of 5.8 μm and axons were manually counted. Axons were identified as rounded white/light-grey objects surrounded by a darker border and no distinction was made among myelinated (very low percentage) and unmyelinated axons. The number of axons was then divided for the size of area exported (axons/unit area) and to obtain the total number of axons per optic nerve the axons/unit area was normalized for the whole area. The whole area of the optic nerves was manually drawn and measured in Fiji by carefully excluding surrounding immune cells and blood vessels.

Image Analysis

Spine density analysis

For spine density analysis, immunostained *C3r KO; Thy1::*EGFP and control brain sections corresponding to prelimbic and cingulate cortices (Bregma: 1.78 to 1.34) were imaged on a TCS SP5 resonant scanner confocal microscope (Leica Microsystems) with a 63x/1.4 oil immersion objective at 48 nm lateral resolution and a z-step of 130 nm. Spine density quantitation was performed as described earlier (5). Briefly, images were deconvolved using Huygens Professional software (Number of iterations<50, quality change threshold – 0.1, theoretical point spread function. Image J software (NIH) was used for semi-automatic quantification of spine density. 8-bit maximum intensity projections were used and only lateral spines were analyzed. Signal intensity was measured in the dendritic shaft and used for normalization across all datasets. Background signal was measured outside the dendritic shaft and 1.4 times the background signal was removed. Images were automatically thresholded using the Huang algorithm. The image was inverted and watershed algorithm was applied followed by clearing of the dendritic shaft and neck. Spine number subsequently analyzed using particle measurement, after sphericity ($>0.3/1$) and size ($>0.005\mu m^2$) thresholding to avoid false positives. Spine density was calculated by normalizing the number of spines to the length of the dendritic branch imaged. On average 7 dendritic branches and 780μm of

117   dendrite was analyzed per animal. Animals from ten different litters were used for spine

118   density analysis.

119   **Quantification of pyknotic cells and microglial phagocytosis**

120   Quantification of pyknotic cells and microglial phagocytosis was analyzed on cortical tissues

121   from postnatal day 5 mice. Stained presumptive cingulate and somatosensory cortical regions

122   were imaged on an Ultraview Vox Spinning Disk Confocal (Perkin Elmer) equipped with an

123   EMCCD Camera (Hamamatsu C9100-50). Initially, the entire slide was scanned at 20x and

124   the region of interest was imaged at higher magnification 60x/1.4NA oil immersion objective

125   with a z-resolution of 0.3µm. Similar imaging parameters were used for both wild-type and

126   knock-out animals. All the analysis was carried out blind to the genotype and phenotype.

127   Quantification of pyknotic cells was performed using Imaris 8.0 or Imaris Viewer (Oxford

128   Instruments) by converting the files to native Imaris file format. Pyknotic nuclei were

129   identified by their distinct bright, condensed nuclei. All the engulfment events were manually

130   confirmed by going through the Z-stack. For quantification of microglial cells, only Iba1

131   positive cells with their soma clearly visible in the field were included. On average 8 fields

132   were analyzed per animal for each brain region. Pyknotic nuclei, phagocytic cups and

133   microglial count were normalized to the volume of tissue used for quantification. Similar

134   volumes were used for quantification of both wildtype and knock-out: ACC total volume:

135   99.2×10^6 um^3 vs 89.7×10^6 um^3 (WT vs KO) and somatosensory cortex total volume: 86.9×10^6

136   um^3 vs 80.6×10^6 um^3 (WT vs KO). Phagocytosis-Apoptosis index was calculated as follows =

137   (proportion of pyknotic nuclei inside microglia)/(density of pyknotic nuclei * density of

138   microglia). Animals from eight different litters were used for this analysis.

139

140

141   **Quantification of Caspase3 cell density**

142   For quantitation of caspase-3 density in *C3r* knockout and control mice, immunostained

143   postnatal day 5 brain sections were imaged on an Ultraview Vox Spinning Disk Confocal

144   (Perkin Elmer) equipped with an EMCCD Camera (Hamamatsu C9100-50). Initially, the

145   entire slide was scanned at 4x and regions of interest were imaged using 40x/1.3NA oil

146   immersion objective with a z-resolution of 0.5µm. Number of aCasp3+ cells were normalized

147   to the volume of the tissue imaged.

148   **Cortical thickness analysis**

149   For cell counting and cortical thickness measurements coronal sections of 30 µm from

150   postnatal day 120 mice were used. Animals from fourteen different litters were used for

151   cortical thickness and cell count measurements. The sections were stained for NeuN and

152   DAPI and imaged on an inverted fluorescence microscope (THUNDER Imaging System,

153   Leica Microsystems) using 20x/0.8 NA objective. The analysis was performed using

154   Fiji/ImageJ, each image was rotated properly to be straight. NeuN channel was used to

155   visualize the white matter structure which was used to identify the reference point for the

156   measurements. Coronal sections from 1.53 mm to 1.21 mm were used for ACC analysis. For

157   measurement of ACC thickness, first, a 180° line was drawn and then moved down until it

158   touches the forceps minor of corpus callosum (fmi). The point in which the line touches the

159   fmi for the first-time structure was used as a reference point. The ACC thickness was

160   measured by drawing a 180-degree line from the reference point until the end of layer 1. Data

161   reported is an average of 3-4 different coronal sections for each animal.

162   For somatosensory cortex analysis, coronal sections from -1.46 mm to -1.57 mm were used.

163   The parameters to measure cortical thickness in somatosensory cortex was experimentally

164   determined to perform the measures always in the S1 region. For measuring the thickness of

165   Somatosensory cortex, as a first step, an 180^0 line was drawn and then rotated at 45 degrees,

166   this line was moved up until it touched for the first time the hippocampus. The point in which

167   the 45-degree line intercepts the beginning of the cortex was used as a reference point from

168   which the 60-degree line was drawn, if the measurement is performed on the right side, and

169   120 degrees if on the left side. This line was extended until the end of the layer 1 and the

170   thickness of the cortex was measured. Data reported is an average of 3-4 different coronal

171   sections for each animal.

172   *Automated cell count using StarDist*

173   The images used for automated cell counting were obtained on an inverted fluorescence

174   microscope (THUNDER Imaging System, Leica Microsystems) using 20x/0.8NA objective

175   using Z-step of 0.85µm and a lateral resolution of 0.41µm. Image acquisition was controlled

176 using LAS X software. All the sections were imaged for NeuN and DAPI channels and
177 similar imaging conditions were used for all the animals. The images were computationally
178 cleared using Large Volume Computational Clearing algorithm (LVCC), a proprietary
179 package of LAS X (Leica Microsystems) before proceeding with counting. LVCC processing
180 helps in reducing the out of focus blurs and background signal.

181 StarDist is a deep supervised machine learning tool developed for automated cell prediction
182 (6). The method is suited for objects with a star-convex shape. When training the StarDist
183 model, the images in the training set are randomly split into training data (90%) and
184 validation data (10%). The validation data is used during the StarDist training to monitor the
185 progress of the training and to determine the best combination of parameters of probability
186 threshold and overlap threshold that allows the best prediction in the validation data. StarDist
187 was trained using the scripts available at https://git.embl.de/grp-bio-it/ai4ia/-
188 /tree/master/stardist. All the models were exported from StarDist using Tensorflow version
189 1.14 and Tensorflow version 1.14.0 was used in Fiji/ImageJ as well. For each model
190 developed the following parameters were determined

191 ● *Probability/Score Threshold* – Higher threshold results in fewer segmented objects,
192 thus reducing chances of false positives.
193 ● *Overlap Threshold* – Higher threshold allows segmented objects to overlap
194 substantially. Allows for segmentation of cells in a crowded field.

195 **Image annotations with QuPath and StarDist training**

196 QuPath v0.2.0-m11 software was chosen for the cell annotations used for all StarDist models.
197 Detailed cell annotations were performed with brush modality only in NeuN channel but
198 DAPI channel of the same image was used for confirmation. The StarDist approach learns
199 how to predict cells using geometric parameters as the distance from the center of the cell to
200 the border of the cell. For the StarDist algorithm, every single signal needs to be annotated
201 even if it is from a cell that is partially visible because for example on the border of the
202 image. Taking this into consideration, annotation was performed in a 512x512 pixels square
203 positioned inside the 600x600 pixels image. Using this approach, it was possible to fully
204 annotate borderline cells even if part of the cell body is going outside the 512x512 pixels
205 square, this approach allows us to maintain the real geometric distance from the center to the
206 border of the cell.

A pipeline outlining development of Stardist based image quantitation is described in **Figure S5A**. We started attempting using a pre-trained model 'Versatile (fluorescent nuclei)'. However, we observed high levels of relative error (%). Then we switched to custom user-trained models. The training was performed using 10 NeuN channel images with 512x512 pixel size from two brain regions: ACC and somatosensory cortex. After training with images from ACC (called 'C cortex' model) and somatosensory cortex (called 'SS cortex' model) we found that the model trained with images from somatosensory cortex ('SS cortex') performed best in automated counting in both ACC and somatosensory cortex regions. In some of the training Data Science Bowl (DSB) was included. DSB is a dataset with 37,333 manually annotated nuclei in 841 2D images from more than 30 experiments across different samples, cell lines, microscopy instruments, imaging conditions, operators, research facilities, and staining protocols. The annotations were manually made by a team of expert biologists (7). Inclusion of DSB pre-training data did not improve the performance of either 'C cortex' or 'SS cortex' model. Training the 'SS cortex' model with DAPI data did not improve the performance of the model. In fact, it resulted in poor performance of the 'SS cortex' model (relative error (%) 4.01±0.30 vs 41.31±20.9 without vs with DAPI) during validation of images from Somatosensory cortex. To improve the performance of the 'SS cortex' model and to eliminate any randomness that might contribute to the performance of the model, using the same training set used in the 'SS cortex' model, 10 different re-trainings were performed. In each training, 10 % of the images were randomly selected and included in the internal validation. Of these new ten re-trained models 'SS cortex re-trained 5' show a decrease of relative error (%) from 4.01±0.30 to 3.18±0.37 ('SS cortex re-trained 5' vs 'SS cortex').

Absolute error = |Number of cells predicted by StarDist − Number of cells obtained by average of 3 counts by manual method|

Relative error in % = (Absolute error / Number of cells obtained by average of 3 counts by manual method) *100

Manual validation of all StarDist models

For manual validation, images of 600x600 pixel from the NeuN channel five each from the ACC cortex and somatosensory cortex were used. For each image, manual counting was performed 3 times and an average of the three values was used as the final measure of the cell count and calculation of relative error (%). The StarDist model was applied to each image

238 and then the result of the predictions was quantified. For each prediction, the relative error

239 (%) was calculated.

Application of the best StarDist model

241 The best model 'SS cortex re-trained 5' was applied to the images using StarDist2D plugin in

242 Fiji/ImageJ, entering manually the parameters of probability threshold and overlap threshold.

243 The model was applied to a 2D z-section chosen with the following criteria: 1) section with

244 the highest intensity; 2) section in which cells are well visible and in focus. In the chosen z-

245 section the analysis was performed in a rectangle drawn with the following criteria: 1) the

246 first dimension was fixed at 300 pixels; 2) the second dimension corresponds to measure of

247 cortical thickness. The Probability/Score Threshold used was 0.45561 and the overlap

248 threshold was set to 0.40000. All the predictions by StarDist were manually verified to

249 remove any false positives or false negatives. The data presented is an average of two

250 sections analyzed per animal.

251 *Retrograde labelling of Callosal projection neurons*

252 **Stereotaxic surgery and retrograde labelling**

253 CTB back-labelling and quantitation was performed as described by De Leon Reyes et al.,

254 2019 (8) with some modifications. Mice of age Postnatal day 30 were anesthetized with 4%

255 Isoflurane and placed in a stereotactic frame (RWD Life Sciences); isoflurane in oxygen (1-

256 2%) was administered to maintain anesthesia. The skin was incised and the skull surface was

257 exposed. The skull was trepanated using a dental drill. Using a glass capillary (tip diameter –

258 30um) 500nl of CTB 647 (0.5% in Phosphate-buffered Saline, Life Technologies) was

259 pressure injected into the Corpus Callosum (Co-ordinates: AP =-1.4, ML =0.70, and DV =-

260 1.70 with an angle of 18^0) at the rate of 50nl/per minute. The capillary was left in position for

261 10-15 minutes after injection and then retracted. Animals received a Carprofen (Rymadil 5

262 mg/kg, subcutaneous injection) as surgical analgesia. After allowing CTB migration for 72 h

263 post-surgery mice were transcardially perfused with 4% PFA in 0.1M Phosphate buffer.

264 **Imaging and analysis of CTB labelled cells**

265 Brains were removed from the skull and left to postfix overnight in 4% PFA at 4°C. Brains

266 were cryoprotected with 30% sucrose and 40 μm coronal sections cut on a cryostat. For

267   quantitative analyses, two coronal sections per animal corresponding to -1.23 to -1.5mm AP

268   were used. Images were acquired with an inverted fluorescence microscope (THUNDER

269   Imaging System, Leica Microsystems) using 20x/0.8 NA objective equipped with an sCMOS

270   camera. Image acquisition was controlled with LAS X software (Leica Microsystems).

271   Images were acquired using 1µm optical thickness and the same imaging parameters were

272   used for all the animals. Mosaics were generated by merging several individual frames, using

273   a spatial overlap of 15% also performed with LAS X software. Quantification of CTB+ cells

274   was performed manually using ImageJ on images from z stacks using DAPI and CTB

275   staining. Analysis was performed in a blinded fashion. S1 and S2 regions of the

276   somatosensory cortex were demarcated by the pattern of CTB back-labeling. Fifty nuclei

277   were randomly selected using the 'multi-point tool' in layer 4 of the S1 and S2 regions. Then

278   the images were switched to CTB channel and proportion of CTB+ cells among the 'selected'

279   nuclei was calculated by going through images in z-stack. Data are presented as the

280   percentage of CTB+ cells out of selected DAPI+ cells. Animals from four different litters

281   were used.

282   ***In vitro electrophysiology***

283   Acute hippocampal slices were prepared as in Basilico et al. 2019 (9). Briefly, *C3r* KO*/C3r*

284   KO*; Thy1*::EGFP male mice at P40 were decapitated under halothane anesthesia and whole

285   brains were rapidly immersed for 5-10 min in chilled artificial cerebrospinal fluid (ACSF:

286   125 mM NaCl, 2.5 mM HCl, 2 mM CaCl$_2$, 1 mM MgCl$_2$, 1.25 mM NaH$_2$PO$_4$, 1.1 mM

287   glucose, 2.6 mM NaHCO$_3$) with 250 mM glycerol. Brains were sectioned into 250-µm-thick

288   slices at 4 ˚C, using a vibratome (DSK, Dosaka EM). Slices were placed in a chamber filled

289   with oxygenated ACSF to recover for 1 hour at room temperature (RT). All recordings were

290   performed at RT on slices submerged and perfused with ACSF with 10 µM bicuculline. CA1

291   pyramidal neurons were visualized with an upright Axioscope microscope (Zeiss) and were

292   patched in whole-cell configuration. Borosilicate glass micropipettes (3.5-4.5 MΩ) were

293   filled with an intracellular solution (135 mM CsMetSO$_4$, 10 mM HEPES, 2 mM MgATP, 0.3

294   mM NaGTP, 2 mM Qx314 bromide, 2 mM MgCl$_2$, 0.4 mM CaCl$_2$, 5 mM BAPTA).

295   Membrane currents were recorded with a patch-clamp amplifier (Axopatch 200A, Molecular

296   Devices) and were filtered at 2 kHz, digitized (10 kHz) and acquired with Clampex 10

297   software (Molecular Devices). To record sEPSCs, each neuron was clamped at -70 mV for 10

298   minutes. Miniature EPSCs (mEPSCs) were recorded after 10 minutes of bath perfusion with

299   tetrodotoxin (TTX, 1 μM). Recorded signals were low-pass filtered at 1 kHz and analyzed

300   using Clampfit 10.4 software (Molecular Devices). 19-21 cells were recorded for sEPSCs and

301   12-14 cells were recorded for mEPSCs. sEPSC were identified on the basis of a template

302   created for each neuron using 50-70 single events for each trace. All events recognized

303   through the template search function were visualized, identified and accepted by manual

304   analysis. To record evoked EPSCs, bipolar theta micropipettes (filled with ACSF) were used

305   for stimulation and placed in stratum radiatum near CA1 area over the Schaeffer-commissural

306   afferent fibers. Input-output curves of eEPSCs were recorded by sequentially stimulating

307   Schaeffer collateral fibers at different intensities (0.1, 0.5, 1, 3, 7 and 10 mA) using paired-

308   pulse protocol (0.1 ms duration of the stimulus, 50 ms interval between two consecutive

309   stimuli and 10 s interval of two pair of stimuli). The experiments were performed from 1 to 8

310   hours after slicing. 19-26 cells were recorded for eEPSCs recordings. The recordings were

311   carried out blind to animal genotype.

312   ***Resting state fMRI***

313   Resting state fMRI (rs-fMRI) experiments were performed as previously described (10–12).

314   At the time of imaging, mice were between 19 and 42 weeks old (wild-type controls: N = 19,

315   age 30±7 weeks; *C3r* knockout: N = 20, age 28±6 weeks, animals from 13 different litters).

316   Briefly, mice were anesthetized with isoflurane (5% induction), intubated and artificially

317   ventilated (2% maintenance). The left femoral artery was cannulated for continuous blood

318   pressure monitoring and terminal arterial blood sampling. After surgery, isoflurane was

319   discontinued and replaced with halothane (0.75%), and fMRI acquisitions commenced 45

320   minutes after isoflurane cessation. Arterial Blood gases (pCO_2 and pO_2), and fluctuations of

321   cortical BOLD-fMRI signal-to-noise ratio (SNR) were measured at the end of functional

322   fMRI acquisitions, and compared between groups in order to discard genotype-dependent

323   physiological confounds and anesthesia sensitivity. Mean pCO_2 and O_2 levels recorded in

324   wild-type controls (22±4 and 210±32 mmHg) and *C3r* knockout (22±5 and 232±27 mmHg)

325   showed no significant differences (2-sample t-test). Body mass and SNR also showed no

326   significant differences between wild-type controls (28.7±5 gm and 20.8±32) and *C3r*

327   knockout mice (28.7±4 gm and 22.1±32), excluding possible confounds from anesthesia

328   depth in our intergroup comparisons (13).

329   rsfMRI images were acquired with a 7.0-T MRI scanner (Bruker Biospin, Milan) as

330   previously described (14), using a 72-mm birdcage transmit coil and a 4-channel solenoid

331 coil for signal reception. For each session, *in-vivo* anatomical images were acquired with a

332 fast spin echo sequence (repetition time [TR] = 5500 ms, echo time [TE] = 60 ms, matrix 192

333 × 192, field of view 2 × 2 cm, 24 coronal slices, slice thickness 500 μm). Co-centered single-

334 shot BOLD rsfMRI time series were acquired using an echo planar imaging (EPI) sequence

335 with the following parameters: TR/TE = 1000/15 ms, flip angle 30°, matrix 100 × 100, field

336 of view 2.3 × 2.3 cm, 18 coronal slices, slice thickness 600 μm for 1920 volumes.

337 *Functional Connectivity Analyses*

338 fMRI images were preprocessed as previously described (11, 12). The first 120 volumes were

339 discarded to allow for T1 and gradient thermal equilibration. Data were despiked, motion-

340 corrected, and spatially registered to an in-house common reference template. Motion traces

341 from head realignment parameters (3 translations + 3 rotations) and the mean ventricular

342 signal were regressed out as nuisance covariates. Denoised data was bandpass-filtered

343 between 0.01-0.1 Hz and spatially smoothed with a full-width at half-maximum kernel of 0.6

344 mm.

345 In order to perform an unbiased investigation of brain regions exhibiting genotype-dependent

346 connectivity alterations, we mapped Local Functional Connectivity (LFC) at the voxel-level.

347 LFC strength here is defined as the averaged Pearson's correlation of a voxel's time-course to

348 a subset of voxels in the local vicinity. We limited this vicinity to connections within a 6-

349 voxel radius, and correlation coefficients were transformed to z-scores using the r-to-z

350 Fisher's transform before averaging, and then back-transformed into correlation mean scores

351 (13). Genotype-dependent LFC differences were assessed at the voxel-level using a 2-tailed

352 Student's t-test and cluster corrected with the family-wise error method (FWER) as

353 implemented by FSL ($|t| > 2$, $p < 0.05$). Quantifications of LFC at the regional level were

354 done by averaging each subject's LFC scores within a region-of-interest (ROI) in the

355 Prefrontal Cortex (PFC) and the mediodrsal Thalamus (TH), and inter-group differences were

356 computed using a 2-tailed Student's t-test ($|t| > 2$, $p < 0.05$) and corrected for multiple

357 comparisons with the Benjamini-Hochberg procedure of False Discovery Rate (FDR) q =

358 0.05. Intergroup differences in the extension and intensity of long-range rsfMRI correlation

359 networks were mapped using a seed-based approach as previously described (15). Genotype-

360 dependent functional connectivity differences to the prefrontal cortex were assessed at the

361 voxel-level using a 2-tailed Student's t-test and cluster corrected with the family-wise error

362 method (FWER) as implemented by FSL ($|t| > 2$, $p < 0.05$). Long-range connections were

363   assessed by computing interhemispheric homotopic connectivity (correlation coefficients)

364   between mirroring cortical Regions of Interest (ROIs, see Figure 4D), or by probing the

365   spatial extension of fMRI connectivity of the ACC using seed-based voxelwise mapping ($|t| >$

366   2, $p < 0.05$) (14). Statistical significance of intergroup correlation strength in each homotopic

367   ROI pair was assessed with a 2-tailed Student's t-test ($|t| > 2$, $p < 0.05$) and corrected for

368   multiple comparisons with the Benjamini-Hochberg procedure of False Discovery Rate

369   (FDR) q = 0.05.

370   ***Statistical analysis***

371   Statistical analysis was performed using either Graphpad 5.0 or Sigmaplot. Plots were

372   obtained with GraphPad Prism 5.0. Each data point refers to an individual animal. The data

373   are presented as mean± SEM. Spine density analysis, retrograde labelling, quantification of

374   apoptotic cells, cortical thickness and cell counts were compared using two-way ANOVA

375   with Tukey's multiple comparison. Axon density, total axon in optic nerve, quantification of

376   microglial engulfment of PSVue and caspase-3 labelled cells were performed with two-tailed

377   Student's t-test or Mann-Whitney test. rs-fMRI data was analyzed by unpaired t-test. We

378   used a 95% CI. A *p* value of <0.05 was set for rejecting the null hypothesis.

379
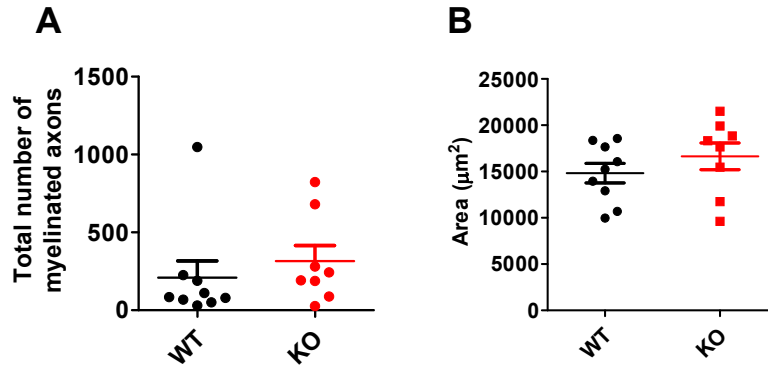
380

381

382

383

384

385

386

387

Supplementary Figures

Figure S1

390   **Figure S1.** *Deficient retinal ganglion cell axonal pruning in C3r knockout mice.* (**A**) No

391   difference in the number of myelinated axons were seen between *C3r* knockout and control

392   littermates (unpaired t-test, p = 0.485). (**B**) A small, non-significant increase in the area of the

393   optic nerve was observed in *C3r* knockout mice (unpaired t-test, p = 0.322; mean ± SEM, * *p*

394   < 0.05, ** *p* < 0.01).
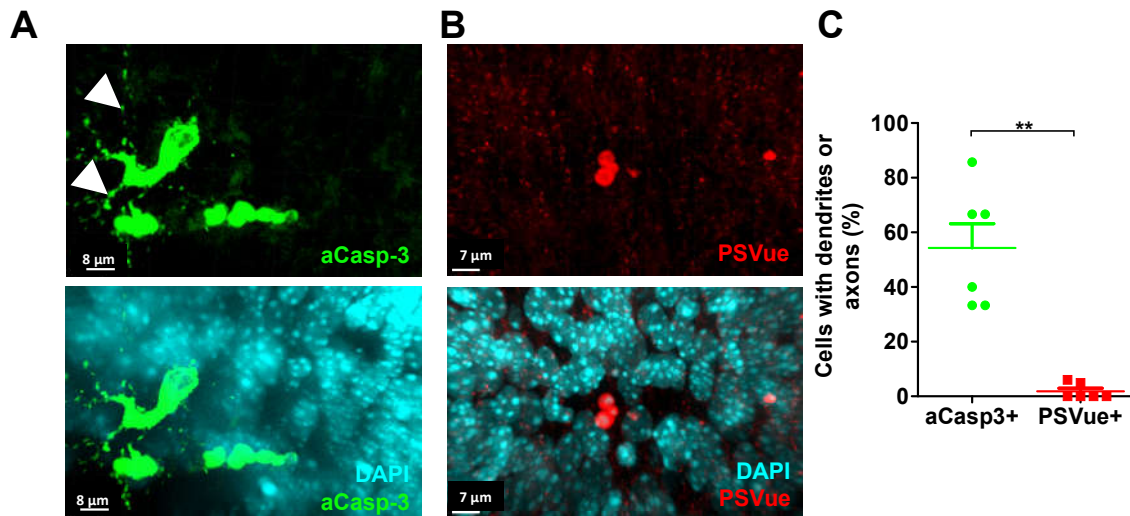
Figure S2

Figure S2. *Microglia phagocytose apoptotic neurons in early postnatal cortex.* (**A**) Activated caspase-3 positive cells (aCasp3+) often exhibit a clear neuronal morphology with blebs of dendrites and axons. (**B**) Unlike aCasp3+ cells, PSVue+ cells do not exhibit clear neuronal morphology. (**C**) Quantitation of aCasp3+ and Phosphatidylserine exposing PSVue+ cells with dendritic branches visible (Mann-Whitney Test, $p = 0.004$; mean ± SEM, * $p < 0.05$, ** $p < 0.01$).
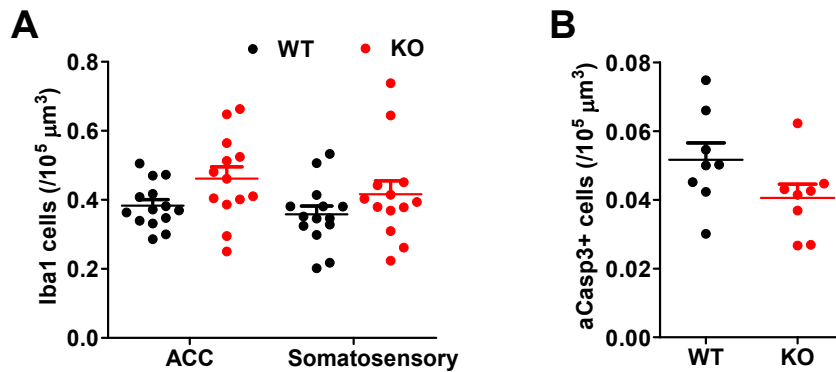
Figure S3. *Deficient neuronal elimination in C3r knockout mice.* (**A**) Marginal increase in the density of microglia is seen in *C3r* knockout mice (two-way ANOVA with Tukey's post hoc test – main effect of region: $F[1, 50] = 1.46$, $p = 0.232$; main effect of genotype: $F[1, 50] = 5.44$, $p = 0.024$; region x genotype interaction: $F[1, 50] = 0.122$, $p = 0.728$). (**B**) Quantification of apoptosis initiation by aCasp3 staining revealed no differences between control and *C3r* knockout mice (unpaired t-test, $p = 0.102$)
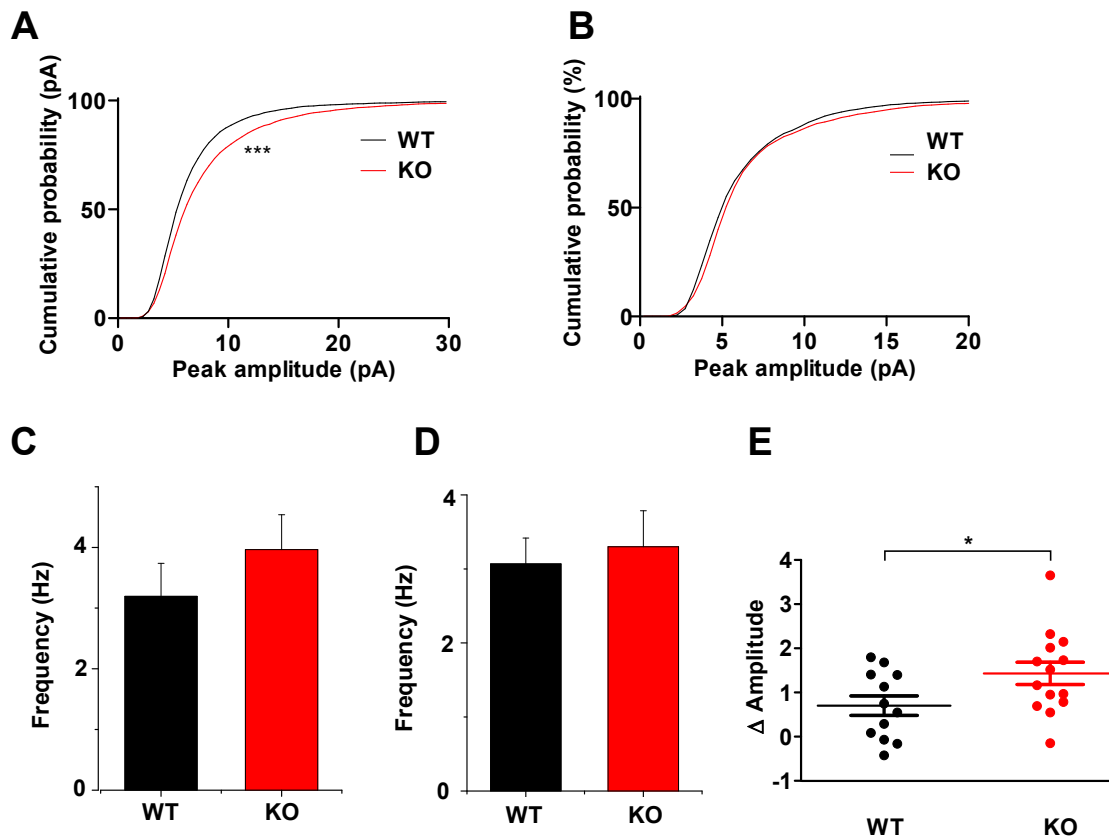
Figure S4. *Increased synaptic connectivity in C3r knockout mice.* (**A**) *C3r* knockout mice show rightward shift in amplitude of sEPSCs compared to wild -ype littermates (Kolmogorov-Smirnov test, p < 0.001). (**B**) No difference in the amplitude of mEPSCs were detected between the two genotypes (Kolmogorov-Smirnov test, p = 0.0597). (**C**) *C3r* knockout mice show no difference in sEPSC frequency compared to wild-type littermates (unpaired t-test, p = 0.34). (**D**) No difference in frequency of mEPSC were detected between the two genotypes (unpaired t-test, p = 0.701). (**E**) Mild increase in Δ amplitude (sEPSC-mEPSC) in *C3r* knockout mice (unpaired t-test p = 0.042; mean ± SEM. * p < 0.05, ** p < 0.01, *** p < 0.001).
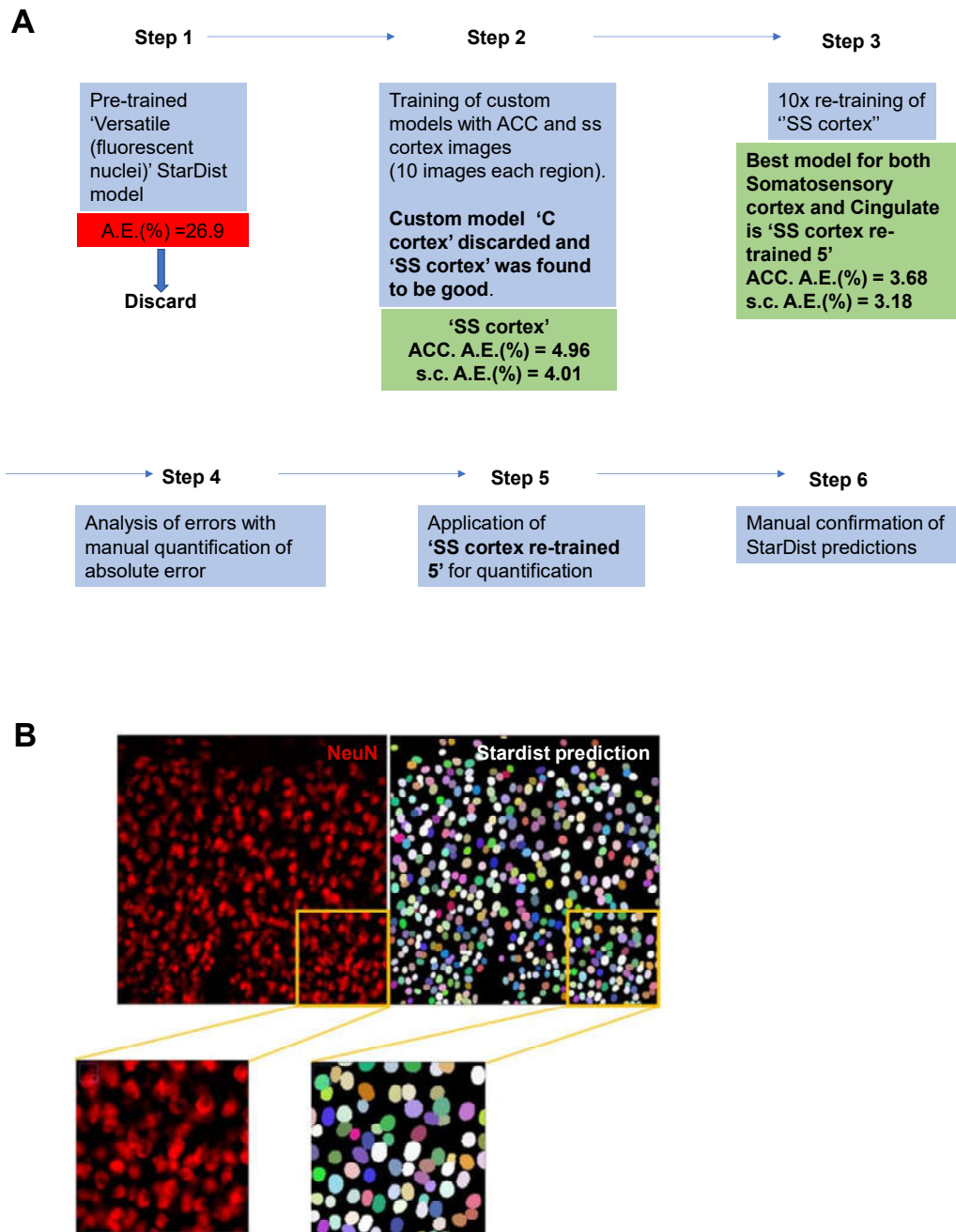
A

Step 1 → Step 2 → Step 3

Pre-trained 'Versatile (fluorescent nuclei)' StarDist model

A.E.(%) =26.9

↓

Discard

Training of custom models with ACC and ss cortex images (10 images each region).

Custom model 'C cortex' discarded and 'SS cortex' was found to be good.

'SS cortex'
ACC. A.E.(%) = 4.96
s.c. A.E.(%) = 4.01

10x re-training of ''SS cortex''

**Best model for both Somatosensory cortex and Cingulate is 'SS cortex re-trained 5'
ACC. A.E.(%) = 3.68
s.c. A.E.(%) = 3.18**

Step 4 → Step 5 → Step 6

Analysis of errors with manual quantification of absolute error

Application of **'SS cortex re-trained 5'** for quantification

Manual confirmation of StarDist predictions

B

NeuN   Stardist prediction

Figure S5

Figure S5. *Development and validation of automated quantification of neurons using Stardist.* (**A**) Flow chart depicting the development and validation of Stardist models for automated quantification of fluorescently labelled NeuN positive cells. (**B**) Example of a Stardist prediction using 'SS cortex re-trained 5' model. All the quantifications from Stardist predictions were manually verified for eliminating false positives and false negatives.

References

1. G. Feng, *et al.*, Imaging neuronal subsets in transgenic mice expressing multiple spectral variants of GFP. *Neuron* **28**, 41–51 (2000).

2. L. Madisen, *et al.*, A robust and high-throughput Cre reporting and characterization system for the whole mouse brain. *Nat. Neurosci.* **13**, 133–140 (2010).

3. A. Coxon, *et al.*, A novel role for the beta 2 integrin CD11b/CD18 in neutrophil apoptosis: a homeostatic mechanism in inflammation. *Immunity* **5**, 653–666 (1996).

4. T. Iwasato, *et al.*, Cortex-restricted disruption of NMDAR1 impairs neuronal patterns in the barrel cortex. *Nature* **406**, 726–731 (2000).

5. L. Weinhard, *et al.*, Sexual dimorphism of microglia and synapses during mouse postnatal development. *Dev. Neurobiol.* **78**, 618–626 (2018).

6. U. Schmidt, M. Weigert, C. Broaddus, G. Myers, "Cell detection with star-convex polygons" in *Medical Image Computing and Computer Assisted Intervention – MICCAI 2018*, Lecture notes in computer science., (Springer International Publishing, 2018), pp. 265–273.

7. J. C. Caicedo, *et al.*, Nucleus segmentation across imaging experiments: the 2018 Data Science Bowl. *Nat. Methods* **16**, 1247–1253 (2019).

8. N. S. De León Reyes, *et al.*, Transient callosal projections of L4 neurons are eliminated for the acquisition of local connectivity. *Nat. Commun.* **10**, 4549 (2019).

9. B. Basilico, *et al.*, Microglia shape presynaptic properties at developing glutamatergic synapses. *Glia* **67**, 53–67 (2019).

10. L. Ferrari, *et al.*, A robust experimental protocol for pharmacological fMRI in rats and mice. *J. Neurosci. Methods* **204**, 9–18 (2012).

11. D. Gutierrez-Barragan, M. A. Basson, S. Panzeri, A. Gozzi, Infraslow State Fluctuations Govern Spontaneous fMRI Network Dynamics. *Curr. Biol.* **29**, 2295–2306.e5 (2019).

12. M. Pagani, *et al.*, Deletion of Autism Risk Gene Shank3 Disrupts Prefrontal Connectivity. *J. Neurosci.* **39**, 5299–5310 (2019).

13. A. Liska, *et al.*, Homozygous Loss of Autism-Risk Gene CNTNAP2 Results in Reduced Local and Long-Range Prefrontal Functional Connectivity. *Cereb. Cortex* **28**, 1141–1153 (2018).

14. A. Liska, A. Galbusera, A. J. Schwarz, A. Gozzi, Functional connectivity hubs of the mouse brain. *Neuroimage* **115**, 281–291 (2015).

15. F. Sforazzini, *et al.*, Altered functional connectivity networks in acallosal and socially impaired BTBR mice. *Brain Struct. Funct.* **221**, 941–954 (2016).